Three-dimensional discrete element modeling of triggered slip in sheared granular media

Behrooz Ferdowsi[*]
Swiss Federal Institute of Technology Zürich, Stefano-Franscini-Platz 5, CH-8093 Zürich, Switzerland
and Swiss Federal Laboratories for Materials Science and Technology, ETH Domain, Überlandstrasse 129, CH-8600 Dübendorf, Switzerland

Michele Griffa[†]
Swiss Federal Laboratories for Materials Science and Technology, ETH Domain, Überlandstrasse 129, CH-8600 Dübendorf, Switzerland

Robert A. Guyer
Solid Earth Geophysics Group, Los Alamos National Laboratory, MS D446, Los Alamos, New Mexico 87545, USA
and Department of Physics, University of Nevada, Reno, Reno, Nevada 89557, USA

Paul A. Johnson
Solid Earth Geophysics Group, Los Alamos National Laboratory, MS D446, Los Alamos, New Mexico 87545, USA

Chris Marone
Department of Geosciences, Pennsylvania State University, University Park, Pennsylvania 16802, USA
and G3 Centre and Energy Institute, Pennsylvania State University, University Park, Pennsylvania 16802, USA

Jan Carmeliet
Swiss Federal Institute of Technology Zürich, Stefano-Franscini-Platz 5, CH-8093 Zürich, Switzerland
and Swiss Federal Laboratories for Materials Science and Technology, ETH Domain, Überlandstrasse 129, CH-8600 Dübendorf, Switzerland

(Received 13 October 2013; published 14 April 2014)

This paper reports results of a three-dimensional discrete element method modeling investigation of the role of boundary vibration in perturbing stick-slip dynamics in a sheared granular layer. The focus is on the influence of vibration within a range of amplitudes and on the fact that above a threshold early slip will be induced. We study the effects of triggering beyond the vibration interval and their origins. A series of perturbed simulations are performed for 30 large slip events selected from different reference runs, in the absence of vibration. For each of the perturbed simulations, vibration is applied either about the middle of the stick phase or slightly before the onset of a large expected slip event. For both cases, a suppression of energy release is on average observed in the perturbed simulations, within the short term following the vibration application. For cases where vibration is applied in the middle of the stick phase, a significant clock advance of the large slip event occurs. In the long term after vibration, there is a recovery period with higher-energy release and increased activity in the perturbed simulations, which compensates for the temporary suppression observed within the short term.

DOI: 10.1103/PhysRevE.89.042204 PACS number(s): 83.80.Fg, 45.70.Ht, 91.30.Px

I. INTRODUCTION

The stick-slip dynamics of a sheared granular layer represents a useful simplified model of how earthquakes unfold on mature strike-slip faults. A fault system accumulates strain energy during interseismic periods, just as a granular layer does during the stick phase. A slip event is the equivalent of an earthquake on a fault [1–3]. A number of recent studies provide evidence that seismic waves radiated by an earthquake can trigger other earthquakes on near and distant faults [4–8]. This phenomenology is termed dynamic earthquake triggering (DET) [9]. An important feature of mature faults is that they contain granular wear material, referred to as fault gouge, within the fault zone [10]. Here we report on an investigation of DET using a granular three-dimensional (3D) discrete element model (DEM) subject to boundary vibrations. We focus on the physical mechanisms of stick-slip and the role of dynamic stresses in triggering stick-slip in a sheared granular layer.

The dynamics of stick-slip is controlled by mechanical and physical properties of the granular gouge, including its confining pressure and shear speed [11,12]. Laboratory scale observations confirm that mechanical vibrations with adequate amplitudes can change the mechanical and frictional properties of the granular layer and thus change its macroscale response. This includes a transition from a solidlike behavior to a transient fluidlike one [13–19]. Johnson *et al*. hypothesized that a similar evolution of mechanical properties due to transient waves is the mechanism responsible for DET [20]. They applied transient sound vibration to sheared granular layers in a double-direct shear experimental setup and found evidence of triggered slip events when the acoustic vibration had amplitudes above a critical threshold [21]. The experiments were carried out using the apparatus developed by Marone *et al*. [22,23], which is capable of capturing a wide spectrum of the dynamic behavior of sheared granular layers, including continuous sliding, intermittent, and quasiperiodic stick-slip dynamics [14,24,25]. Johnson *et al*.

[*]behroozf@ethz.ch; behrooz.ferdowsi@empa.ch
[†]michele.griffa@empa.ch

observed that when vibration amplitudes corresponding to strains greater than 10^{-6} are applied at the shear stress levels of approximately 95% of the failure strength, a cascade of small slip events is triggered followed by a delayed larger event. The existence of a dynamic strain amplitude threshold is indeed in agreement with the earth-scale observational studies for several dynamically triggered earthquakes (and aftershocks) [26]. Other studies also demonstrate the existence of threshold values of strain amplitude for dynamic earthquake triggering. The existence of a unique threshold strain value is an important open question, however, there is increasing evidence that in many cases DET may be governed by a threshold mechanism [27–29]. Despite the richness of experimental observations confirming the signatures of DET at laboratory scale, it still remains an open question how the small amplitudes of dynamic strain can cause triggering with regard to the grain-scale physics of the granular layer. Moreover, it is important to know if the consequences of dynamic slip triggering depend on when the vibration (or triggering source) is being applied during the stick phase [14].

We previously investigated the role of boundary vibration on triggered slip by studying the affine and nonaffine deformation fields [30,31] within the granular layer and by tracking their spatiotemporal evolution. The studies were carried out by implementing a 2D DEM model of a sheared granular layer [32,33]. These studies showed that vibration itself introduces large affine and nonaffine strains, which lead to the initiation of slip at lower shear stress than an equivalent slip event without vibration. Our prior work also showed that a primary effect of boundary vibration and dynamic stressing was a clock advance of a stick-slip event compared to the onset time for the event in the reference model, which is consistent with seismological studies of dynamic triggering on earthquake faults [34]. However, these earlier works focused on the immediate influence of vibration, within the vibration interval [32,33,35] or only for the next expected large slip event to occur [34]. This paper extends the analysis to the triggering effects beyond the vibration interval, from a statistical point of view. The question is whether DET produces only a clock advance of a single event or the overall stick-slip dynamics changes, from a statistical point of view, after vibration application. Moreover, the three dimensionality of the present simulations adds new features in the model including significant precursory activity, creeplike behavior before slip events, and delayed triggering, i.e., triggering of a slip event long after vibration is removed, but still before the original slip event onset, so yet with a clock advance. These features were not present in our previous 2D simulations. However, both the precursory activity and delayed triggering are frequently observed in the authors' experimental setup at the Pennsylvania State University [21,36]. Three-dimensional simulations are therefore closer to the behavior observed in the experiments.

Here we report results of 3D DEM simulations of triggered slip in sheared granular media. We investigate the effect of boundary vibration on spontaneous stick-slip dynamics. We begin by describing the modeling approach and basic metrics that are used for monitoring system behavior. Then we show the influence of boundary vibration on stick-slip dynamics by varying the vibration amplitude and evaluate the possible existence of a critical vibration amplitude for triggering. We demonstrate the short- and long-term influences of a triggering vibration amplitude on the granular energy release during slip. Vibrations are applied either in the middle of the stick phase or slightly before the onset of the spontaneous large slip event. We start with two specific examples and then present statistical analysis of the results for 30 triggered slip events.

II. MODEL DESCRIPTION

Figure 1 illustrates the simulated granular fault gouge. The model consists of three main units: a driving block at the top, a granular (gouge) layer in the middle, and a substrate block at the bottom, each defined by particles. The driving and substrate blocks are used to confine the granular gouge by applying a constant normal force in the Y direction. The top driving block moves at constant velocity in the positive X direction and applies a shear force to the granular gouge layer.

Each variable or parameter in our 3D DEM model is expressed in terms of the following basic dimensional units: $L_0 = 150\ \mu$m, $t_0 = 1$ s, and $M_0 = 1$ kg, for length, time, and mass, respectively. Here L_0 represents the largest particle radius within the overall DEM model.

The driving and substrate blocks are modeled as systems of spherical bonded particles. The structure of these two blocks allows for dynamic interaction with the granular gouge layer during shear, analogous to tectonic blocks in a fault system. The driving and substrate blocks consist of two sublayers. The first sublayer [top layer (brown colored particles) for the driving block and bottom layer (red colored particles) for the substrate block] consists of a hexagonal-close-packed (hcp) arrangement of particles with radius L_0. This layer ensures the flexural rigidity of the driving and substrate blocks, while allowing elastic deformation and dynamic interaction. The second sublayer [roughness layer (dark and light blue colored particles)] consists of particles with radii distributed within $[0.3; 1.0]L_0$. These roughness layers are meant to increase the roughness in the interaction of the driving block or substrate with the granular gouge layer [37]. A periodic boundary condition is employed in the X direction and the length of the system in the X direction is $70L_0$. The driving and substrate

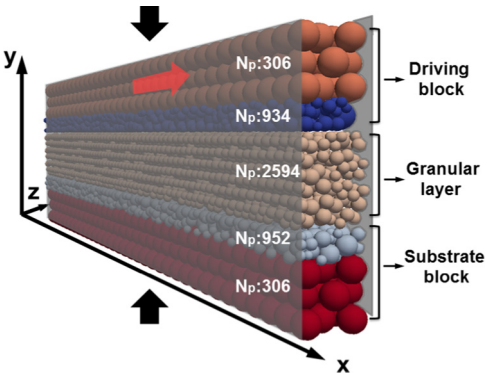

FIG. 1. (Color online) The 3D DEM model comprised of the driving block (top), a granular gouge layer (center), and a substrate block (bottom).

blocks have thickness in the Y direction of approximately $7.0L_0$. Furthermore, the ratio between the roughness layer thickness and the hcp layer thickness is about 0.32. The particle interaction of both the hcp and roughness layers is modeled by radial springs [38,39]. The interparticle radial force is $F_r = K_r \Delta r$. Here Δr is the overlap value of two particles $\Delta r = (r_1 + r_2) - d$, where d is the distance between the two particles and $r_1 + r_2$ is the sum of the two particles' radii. The radial compressional or tensional spring stiffness K_r is $2.9775 \times 10^7 M_0 t_0^{-2}$.

The granular gouge layer consists of a set of spherical unbonded particles with radius $[0.35; 0.55]L_0$. The initial thickness of the granular layer in the Y direction, L_Y, (orthogonal to the Z direction) is $6.25L_0$, which is $L_Y \approx 7d$, where d is the average size of the granular gouge layer particles. This size is enough for a jamming-unjamming transition in the layer [40]. The thickness in the Z direction, L_Z, (orthogonal to the Y direction) is chosen as $5.46L_0$, which is $L_Z \approx 6d$. We verified that the stick-slip dynamics and its statistical features remain unchanged for $L_Y \geqslant 6d$ and $L_Z \geqslant 6d$ and that the system-spanning slip events are observed in all these simulations. For more information on the analysis performed on the size sensitivity of the simulations, we refer to the supplemental materials of an earlier paper published by the authors about our reference simulations [41]. The granular gouge layer particles interact with each other and with particles of the driving block or substrate via a repulsive Hookean spring with radial and tangential components that represent normal (to the contact plane) and frictional forces, respectively [38,39]. The radial component has a spring stiffness $K_r = 5.954 \times 10^7 M_0 t_0^{-2}$. The spring stiffness of the tangential component is $K_s = 5.954 \times 10^7 M_0 t_0^{-2}$. The frictional interaction among the granular gouge particles is implemented similarly to the model proposed by Cundall and Strack [42]. The tangential contact force is chosen as the minimum value of $K_s \Delta s$ and the Coulomb threshold value μF_r, at each time step, where Δs is the tangential component (to the contact plane) of the particles displacement and μ is the friction coefficient between the two particles' surfaces and can be either static μ_s or dynamic μ_d. We chose friction coefficient values of $\mu_s = \mu_d = 0.4$ to produce a macroscopic frictional behavior corresponding to quartz sand aggregates. The frictional interaction between the granular gouge particles and the roughness layers' particles is modeled in the same way with the friction coefficients of $\mu_s = \mu_d = 0.7$. These values were selected based on a parametric study to enhance the stick-slip behavior by increasing the frictional interaction at the interface between the two layers.

The particle assemblies of the roughness layers as well as of the granular gouge layer were initially generated using a space-filling particle insertion method [43]. There are totally 5092 particles in the model. The number of particles in each layer is noted in Fig. 1. The type of packing algorithm and the chosen size range for the granular gouge particles result in a quasiuniform particle size distribution. Figure 2 shows the particle size distributions of both the roughness and granular gouge layers. The walls orthogonal to the Z direction have frictionless elastic repulsive interactions with the particles. These walls have the same elastic stiffness as of the granular gouge layer particles. In the Y direction, the first rows of the

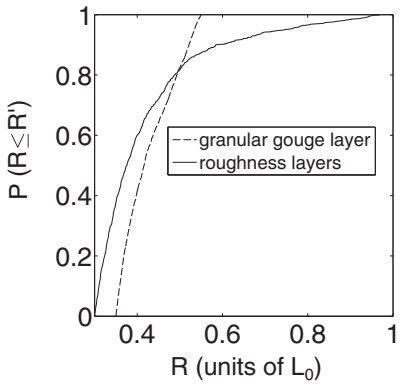

FIG. 2. Particle size distribution (PSD) of the roughness layer of driving block and substrate and the granular gouge layer.

hcp layers' particles (those particles in contact with the walls) of the driving and substrate blocks are bonded (attached) to the walls to transfer the shear loading efficiently from the walls to the granular gouge layer. These Y-direction walls have also the same elastic stiffness of the particles in contact with them.

Each simulation run consists of two stages. During the first stage, the consolidation stage, no shear load is imposed and the granular gouge layer is compressed by the vertical displacement of both the driving block and the substrate. The displacement continues until the applied normal stress on the granular gouge layer equals the desired value of $\sigma_n = 40$ MPa. The second stage of each simulation run starts after the consolidation stage and consists in keeping the normal load constant on the driving block while applying a constant velocity of $V_{X,0} = 0.004 \frac{L_0}{t_0}$ to the top particles of the driving block. The imposed velocity introduces a shear load to the granular system. A ramp protocol is employed for gradually increasing the shear velocity from 0 to $V_{X,0}$ [32–34]. The confining pressure and shear velocity are found to be among the most important parameters determining the type of dynamical regime of the granular layer [44]. The shear velocity and confining pressure have been selected after a parametric study to identify the pair values of confining pressure and shear velocity (σ_n-$V_{X,0}$) that lead to stick-slip dynamics. The simulation parameters have been selected to achieve stick-slip dynamics and then use this to investigate microscopic mechanisms of slip triggering. The values that are used here are not aimed to represent totally real scale observations but to provide the same global characteristics.

The simulations that are not exposed to any vibration are called reference runs, while the simulations with vibration are called perturbed runs. In the specific case of the perturbed (also called triggered) runs, i.e., when external vibration is applied, an additional boundary condition consists in imposing a displacement in the Y direction for the bottom particles of the substrate. The temporal displacement of this boundary displacement is modeled as

$$u_Y(t) = A\Delta t\left[\frac{\partial f}{\partial t}(t,t',T_v,\tau)\cos\left(\omega(t-t')-\frac{\pi}{2}\right)\right.$$
$$\left.-\omega f(t,t',T_v,\tau)\sin\left(\omega(t-t')-\frac{\pi}{2}\right)\right], \qquad (1)$$

where

$$f(t,t',T_v,\tau) \equiv \frac{1}{2}\left[\tanh\left(\frac{t-t'}{\tau}\right) - \tanh\left(\frac{t-(t'+T_v)}{\tau}\right)\right]. \quad (2)$$

In Eqs. (1) and (2), $t = m\Delta t\ \forall m = 0,1,\ldots$, is discretized time and Δt is the simulation time step. Equation (1) represents a sinusoid with angular frequency $\omega = 2\pi f_0$, with $f_0 =$ 1 kHz, whose amplitude is modulated in time by a waveform with a Gaussian-like shape, given by Eq. (2). This vibration frequency is the minimum sound frequency of vibration in the laboratory experiments by Johnson *et al.* [21]. In Eq. (1), t' represents a phase shift term for centering the temporal window of the vibration at different times during the stick-slip dynamics. We use $\tau = 0.01$ and $T_v = 0.02$ in Eq. (2) and they play, respectively, the roles of a rising or decaying time constant and width for the displacement waveform. In Eq. (1), A is the the vibration peak amplitude value.

For the implementation of the model, we used the open source code ESYS-PARTICLE, developed at and maintained by the Earth Systems Science Computational Center of the University of Queensland, Brisbane, Australia. ESYS-PARTICLE solves Newton's equations of motion for the center of mass of each particle by a first-order explicit finite difference scheme and for the rotation angles about the center of mass by a finite difference rotational leapfrog algorithm [45]. The finite difference time step $\Delta t = 15 \times 10^{-6} t_0$ is small enough to guarantee numerical stability and to satisfy the sampling theorem for a vibration signal with maximum frequency $f_{\max} =$ 20 kHz. We initially use a range of vibration amplitudes that includes $A = \{1,10,20,30,40,50,60,70,80,90,100\} \times 10^{-7} L_0$.

The stick-slip behavior of the granular gouge layer is monitored by its friction coefficient time series. The friction coefficient μ is defined as the ratio of shear stress developed at the boundary layers to the imposed normal stress. The size of a slip event is calculated based on the kinetic energy released during slip by the granular gouge layer during the event occurrence. The kinetic energy of each jth particle belonging to the granular gouge layer K_j is defined as $K_j = K_j^{\text{trans}} + K_j^{\text{rot}}$, where K_j^{trans} is the jth particle translational kinetic energy and K_j^{rot} is its rotational kinetic energy. We define the total kinetic energy for the overall granular gouge layer as $K_{\text{tot}} \equiv \sum_{j=1,\ldots,M} K_j$, with M the total number of granular layer particles. At the onset of a slip event, the kinetic energy increases sharply from the background level. The largest increase in the kinetic energy, which originates from the loss of potential energy stored in particle contacts, occurs at the moment of a slip event. The total energy released during a slip event with a length of N time steps of size Δt is defined as $E = \sum_{i=1}^{N} (K_{\text{tot}} - K_{\text{tot},0})\gamma \Delta t$, where γ is the shear strain rate of the driving block, which is calculated as the temporal derivative of the ratio between the driving block top layer displacement and the granular gouge layer thickness (units t_0^{-1}). The shear strain rate is nearly constant over the time period of a slip event and is used to obtain the correct units of energy for E after the integration in time.

As mentioned earlier, we have described the basic behavior of our reference 3D DEM model stick-slip behavior in an earlier work [41]. The packing fraction in the simulation is $\sim$0.58 at the beginning of stick phases and the packing fraction gradually decreases while the granular layer dilates during the stick-phase phase to $\sim$0.56. In our model, we call those slip events with $E \geqslant 1 \times 10^{-6} M_0 L_0^2 t_0^{-2}$ large slip events. The distribution of large slip events in our model follows a power law with $\beta \simeq 1.23$. The β value complies with observationally found values for earthquakes [46–48]. In addition, large slip events in our 3D DEM model are preceded by a sequence of small slip events, microslips, whose occurrence increases exponentially before the large slip event onset [41].

III. RESULTS

Figure 3(a) shows the friction coefficient time series μ for a reference (black line) and its corresponding perturbed runs (colored lines) for a range of vibration amplitudes. The vibration interval is illustrated with vertical dashed lines and a gray box. The reference run time window shows the stick phase of a large slip event happening at $t = 248.7 t_0$. This figure shows that vibration amplitudes $A < 6 \times 10^{-6} L_0$ do not change the time location of the large slip event, while vibration amplitudes $A \geqslant 6 \times 10^{-6} L_0$ cause a significant clock advance of the large slip event in the perturbed runs compared to the reference run. The other interesting feature of triggering shown in this figure is a reduction of the friction coefficient during the vibration interval for vibration amplitudes $A \geqslant 2 \times 10^{-6} L_0$. We refer to this friction reduction during the vibration interval as frictional weakening. We investigated this phenomenon in detail in an earlier work [35]. The current study is focused on the triggering influence on the next upcoming large slip event.

The kinetic energy signal for the reference and perturbed runs are shown in Fig. 3(b). During a large slip event, the kinetic energy abruptly increases above its background level. This corresponds to a transfer of energy from the elastic potential energy to the kinetic. For vibration amplitudes $A < 6 \times 10^{-6} L_0$, there exists a mild and temporary decrease of the friction coefficient during the vibration interval. However, the friction coefficient value goes back to its background value following the end of the vibration and the reference large slip event takes place with almost no clock advance. For $A \geqslant 6 \times 10^{-6} L_0$, the large slip event takes place with a clock advance and an energy release smaller than the reference large slip event.

To explore the granular contact network rearrangement and its possible implications for triggering influence, we look at the ratio of sliding contacts in the granular layer [49]. We show in Fig. 3(c) the ratio of the number of slipping contacts to the total number of contacts in the granular gouge layer, called the slipping contact ratio (R_{SC}), for the reference and perturbed runs. Slipping contacts are those contacts that reach the grain-scale dynamic friction μ_d in contrast to the sticking contacts that maintain the grain-scale static friction μ_s. The grain-scale dynamic friction regime occurs when a contact tangential force exceeds the product of the static friction coefficient and the normal contact force ($F_t > \mu_s F_r$). For the reference run, at the beginning of the stick phase, the R_{SC} is about 0.01. As the macroscopic friction coefficient increases, the shear force between the particles increases, hence the R_{SC} increases until it reaches a value of about 0.04. From this level on, the R_{SC} slightly and gradually increases until it reaches a

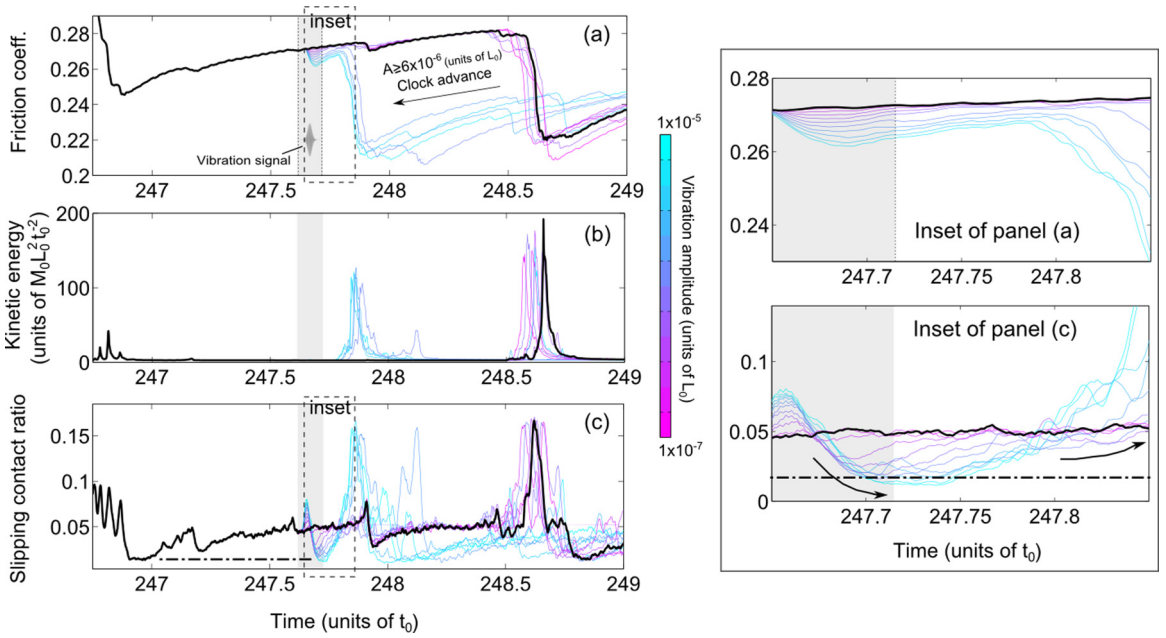

FIG. 3. (Color online) Triggering influence with an increase of the vibration amplitude: time series of (a) friction coefficient, (b) total kinetic energy, and (c) slipping contact ratio. Two insets for (a) and (c) show a more detailed look at the signals during and shortly after the vibration interval. The vibration interval is indicated by vertical dashed lines and a shadowed area in all panels. Black lines in all panels refer to the reference run, while colored lines refer to perturbed runs with a range of amplitudes shown in the figure's color bar.

critical value of about 0.06, where the large slip event takes place. The R_{SC} is a measure of the critical shear loading of the granular layer, showing which portion of contacts are fully mobilized. The critical R_{SC} value controls the lower bound of the isostatic coordination number for frictional packings, therefore its increase forces the medium from a marginally (shear-)jammed to unjammed state [50–52]. Following the start of the vibration interval, the R_{SC} begins to increase even with quite small boundary vibrations, in correspondence with the frictional weakening and destabilization or mobilization of the granular layer. The R_{SC} reaches a maximum at about the peak of the vibration displacement signal. After the vibration interval, the granular layer stabilizes, which is accompanied by first a decrease in R_{SC} and then an increase in the background level due to shearing. After this period, the R_{SC} value recovers slowly back to its reference level and trajectory for small amplitudes $A < 6 \times 10^{-6} L_0$. However, for large amplitudes $A \geqslant 6 \times 10^{-6} L_0$, when the R_{SC} value decreases to a value lower than its value at the beginning of the stick phase[1] (shown by a dashed line), it does not go back to the reference level after the vibration has stopped. The decrease of R_{SC} is then followed by an increase much higher than the background level (above the values achieved in the stick phase, $R_{SC} > 0.06$), which leads to instability and the granular layer cannot sustain its current shear stress level for long.

We can estimate the strain induced by the vibration as $\epsilon = \frac{A}{\lambda}$, where ϵ is the induced strain, A is the vibration amplitude in the unit of L_0, and λ is the wavelength. The wavelength is $\lambda = \frac{c}{f}$, where c is the sound speed and f is the vibration frequency. The sound speed is approximately $c = \sqrt{K/\rho}$. Here the density of the granular layer is $\rho \approx 1.8339 \times 10^{11}$ kg/m^3,[2] while the bulk modulus K is measured to be about 10 GPa. The strain induced by a specific vibration amplitude, e.g., $A = 6 \times 10^{-6} L_0$, is then approximately equal to

$$\epsilon = \frac{A}{\lambda} = \frac{(6 \times 10^{-6})(1.5 \times 10^{-4})}{\left(\frac{0.2335}{10^3}\right)} = 3.9 \times 10^{-6}.$$

With similar calculations, vibration amplitudes in the range of $A = (1 \times 10^{-7}, 1 \times 10^{-6}, 2 \times 10^{-6}, \ldots, 4 \times 10^{-5}) L_0$ correspond approximately to the strain range of $\epsilon = (0.64 \times 10^{-8}, 0.64 \times 10^{-7}, 1.28 \times 10^{-6}, \ldots, 2.56 \times 10^{-5})$.

So far we have explained by an example the influence of triggering, within a range of amplitudes, on the short-term spontaneous stick-slip behavior. We now move on to compare the behavior of the perturbed run with the reference run, in

[1]Note that this decrease in R_{SC} is far beyond the decrease of the friction coefficient if compared to the corresponding values of both signals (R_{SC} and friction) at the beginning of stick phase.

[2]The density of the granular layer ρ is calculated as the ratio of the mass of the total number of particles to the volume of the granular gouge layer at its sheared confined state. The density of a single particle in our DEM model ρ_s is chosen as 2.9×10^{11} kg/m^3. The choice of ρ_s is based on a density scaling scheme [53–55] that is frequently used in DEM modeling studies to increase the simulation time step ($\Delta t \propto \sqrt{\rho_s}$) and to make the simulations computationally feasible. At the same time, we checked that the inertia number [56–58] of the DEM runs is always below 10^{-6} to ensure that the behavior remains in the quasistatic regime and the density scaling effects would be negligible.

both the short and long term after the application of vibration. The vibration interval is applied either at about the middle of the stick phase or very close to the onset of a large slip event. We investigated both types of vibration applications for 30 distinct large slip events. We use vibration amplitude $A = 7 \times 10^{-6} L_0$, large enough to cause a clock advance in an upcoming large slip event.

A. Vibration about the middle of the stick phase

Figure 4(a) shows the friction coefficient signal for the reference run (black line) and a perturbed run (blue line) as an example for the case when vibration is applied at about the middle of the stick phase. We use a normalized time (to failure): $t_{\text{norm}} = -1$ corresponds to the beginning of the stick phase of a reference slip event, while $t_{\text{norm}} = 0$ corresponds to the time the slip or failure takes place in the reference run. The vibration interval center is shown with an arrow in the figure. The vibration amplitude is $A = 7 \times 10^{-6} L_0$ and, as expected from the earlier observations, it induces a clock advance in the upcoming large slip event. Figure 4(b) illustrates the kinetic energy signal for these reference and perturbed runs. This figure indicates that the energy release of the triggered slip event is less than the energy release of the upcoming slip event in the reference run. The cumulative energy release is defined as $\tilde{E}(t) = \sum_{i=1}^{M} E_i$, where M is the number of events included in the time interval $[0; t]$ and E_i is the energy release of event with number i. The evolution of $\tilde{E}(t)$ in the reference

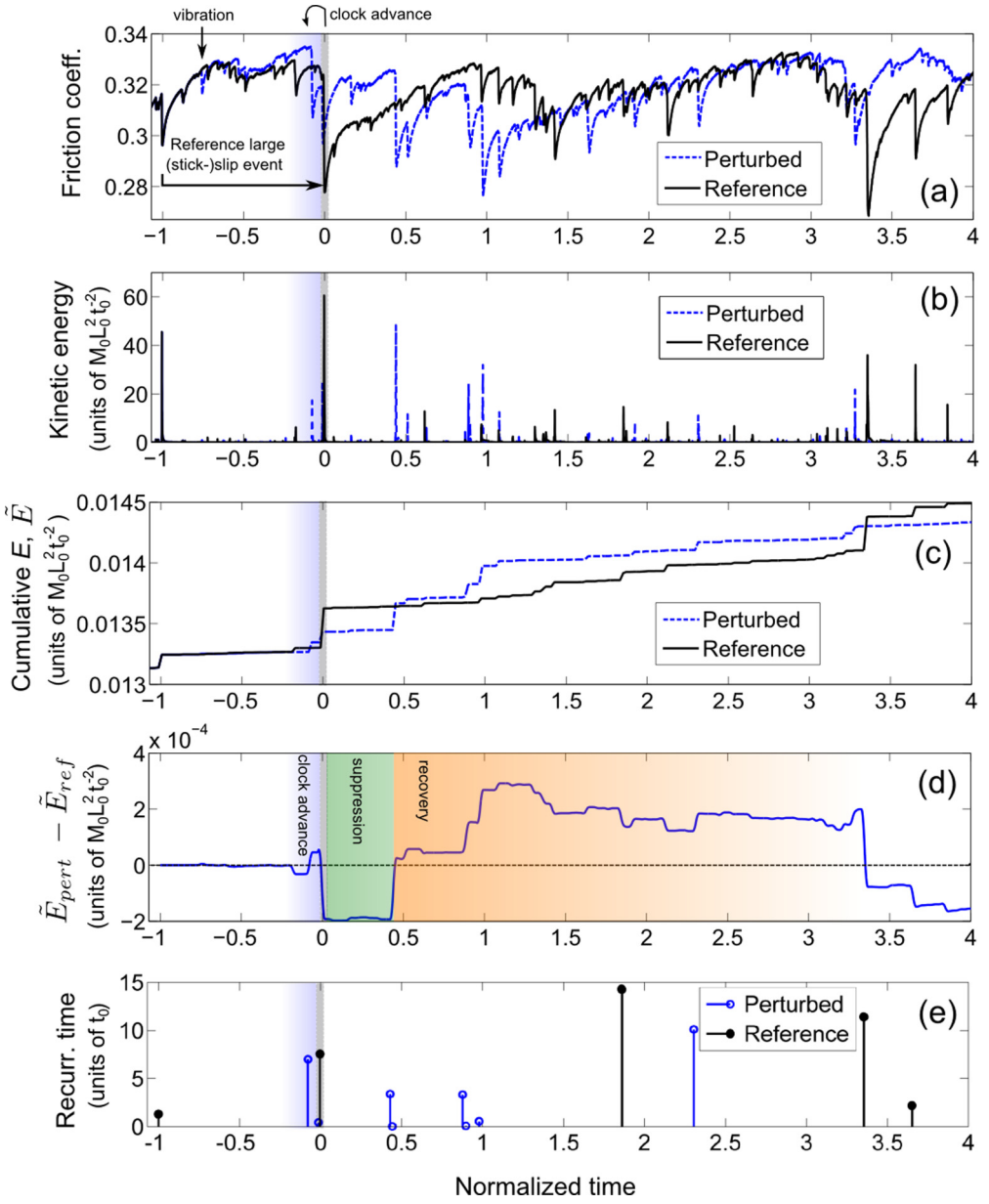

FIG. 4. (Color online) Characteristic behavior when vibration is applied at about the middle of the stick phase: (a) friction coefficient signal, (b) total kinetic energy signal, (c) cumulative energy release $\tilde{E}(t)$ for the reference and perturbed runs, (d) difference between the cumulative energy release of the perturbed run and that of the reference run ($\tilde{E}_{\text{pert}} - \tilde{E}_{\text{ref}}$), and (e) recurrence time for slip events with $E \geqslant 5 \times 10^{-7} M_0 L_0^2 t_0^{-2}$. The vibration amplitude is $A = 7 \times 10^{-6} L_0$.

and perturbed runs is plotted in Fig. 4(c). The difference between the cumulative energy release of the perturbed run and the reference run ($\tilde{E}_{\rm pert} - \tilde{E}_{\rm ref}$) is presented in Fig. 4(d). Figure 4(d) demonstrates the clock advance in the energy release of the perturbed run, followed by a temporary suppression of energy release. The suppression of energy release is due to the earlier and smaller events in the perturbed run. This suppression of energy release does not last for a long time (in this example it lasts until $t_{\rm norm} \approx 0.5$), as shortly there will be a series of slip events that compensates for the suppression and brings the value of $\tilde{E}_{\rm pert} - \tilde{E}_{\rm ref}$ to positive levels. This means there is more energy release in the perturbed run compared to the reference for a certain amount of time $0.5 < t_{\rm norm} < 3$. We call this interval in the perturbed run the recovery period from the initial suppression.

Figure 4(e) shows the interevent time, also called recurrence time, for slip events with size $E \geqslant 5 \times 10^{-7} M_0 L_0^2 t_0^{-2}$ in the reference and perturbed runs. The $E = 5 \times 10^{-7} M_0 L_0^2 t_0^{-2}$ corresponds to the middle size range of the smallest events that show some precursory activity in our 3D DEM model [41]. The selection of $E \geqslant 5 \times 10^{-7} M_0 L_0^2 t_0^{-2}$ ensures that all events that have some precursory activity, which thus result from significant shear loading of the granular layer, are included. This figure indicates that during $0.5 < t_{\rm norm} < 1$, slip events take place successively in the perturbed run. These slip events in the perturbed run have recurrence time smaller than the slip events that take place in the reference run during the same time interval.

We performed the same type of triggering simulations (vibration amplitude $A = 7 \times 10^{-6} L_0$) for 30 large events selected from different independent reference runs with different initial particle position. The average $\tilde{E}_{\rm pert} - \tilde{E}_{\rm ref}$ signal for these 30 large events is presented in Fig. 5(a). The results, similar to the example described above, show a clock advance of the large events, on average, followed by a suppression of energy release until $t_{\rm norm} \approx 3$. The suppression of energy release is compensated for later on by a period of higher energy release and activity, termed recovery, in the perturbed runs compared with the reference runs. The recovery period can on average last until $t_{\rm norm} \approx 5$ in the perturbed runs.

For each time step, the number of realizations where $\tilde{E}_{\rm pert} - \tilde{E}_{\rm ref} > 0$ and $\tilde{E}_{\rm pert} - \tilde{E}_{\rm ref} < 0$ are defined as $N_{\rm pos}$ and $N_{\rm neg}$, respectively, and $N_{\rm tot} = 30$ is the total number of realizations. The ratios of $\frac{N_{\rm pos}}{N_{\rm tot}}$ and $\frac{N_{\rm neg}}{N_{\rm tot}}$ as a function of normalized time are shown in Figs. 5(b) and 5(c), respectively.

The three stages (clock advance, suppression, and recovery) can be characterized based on the $\frac{N_{\rm pos}}{N_{\rm tot}}$ and $\frac{N_{\rm neg}}{N_{\rm tot}}$ variations in time. (i) During the clock advance time interval ($-0.5 < t_{\rm norm} \leqslant 0$), the majority (60%–80%) of realizations show a constantly higher energy release in their perturbed runs. (ii) In the suppression time period ($0 < t_{\rm norm} \leqslant 3$), more than 90% of the realizations show an abrupt energy suppression immediately after $t_{\rm norm} = 0$. As we get farther from $t_{\rm norm} = 0$, the intensity of the energy suppression gradually decreases and the probability of $\frac{N_{\rm neg}}{N_{\rm tot}}$ declines to around 55%. (iii) During the recovery time interval ($3 < t_{\rm norm} < 5$), the probabilities of positive and negative values of $\tilde{E}_{\rm pert} - \tilde{E}_{\rm ref}$ gradually become equal and fluctuate around 50%. However, the positive values

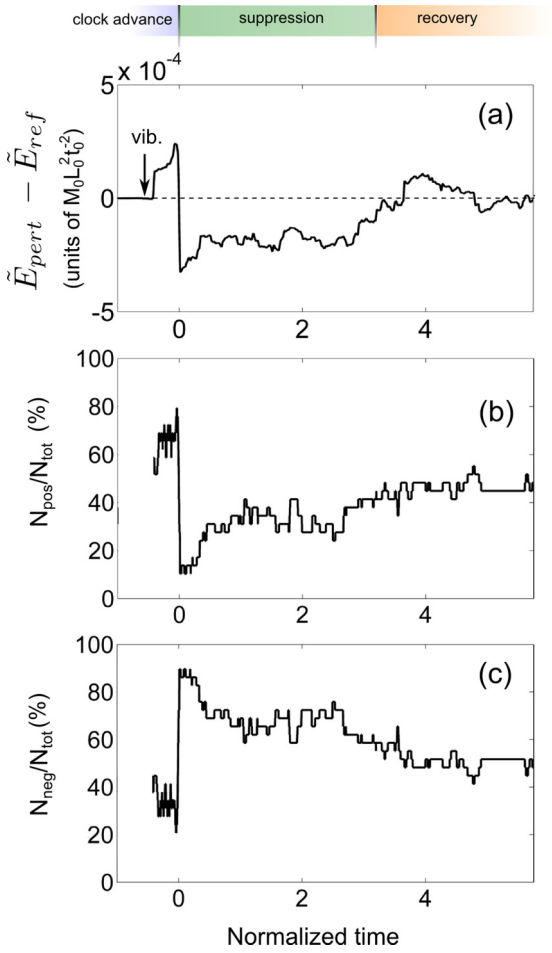

FIG. 5. (Color online) (a) Average results of the difference between the cumulative energy release of the perturbed run and that of the reference run ($\tilde{E}_{\rm pert} - \tilde{E}_{\rm ref}$) for 30 triggered large events when vibration is applied at about the middle of the stick phase for each case (arrow shows the approximate location of vibration in the perturbed runs). The vibration amplitude is $A = 7 \times 10^{-6} L_0$. (b) Percentage of realizations $\frac{N_{\rm pos}}{N_{\rm tot}}$ where $\tilde{E}_{\rm pert} - \tilde{E}_{\rm ref} > 0$. (c) Percentage of realizations $\frac{N_{\rm neg}}{N_{\rm tot}}$ where $\tilde{E}_{\rm pert} - \tilde{E}_{\rm ref} < 0$.

of $\tilde{E}_{\rm pert} - \tilde{E}_{\rm ref}$ are larger than the negative ones, which result in a positive average value of $\tilde{E}_{\rm pert} - \tilde{E}_{\rm ref}$.

Figures 6(a) and 6(b) show the complementary cumulative distribution function G of event size [Fig. 6(a)] and recurrence time [Fig. 6(b)] for slip events with $E \geqslant 5 \times 10^{-7} M_0 L_0^2 t_0^{-2}$ during the suppression period in the perturbed and reference runs for 30 triggered large events. The recurrence time statistics follow an exponential distribution with $G(T_R) = e^{-T_R/\tau}$, where T_R is the recurrence time and τ is the average recurrence time of the distribution. The exponential distribution for recurrence time statistics is characteristic of a Poisson process. The average recurrence time τ increases from $\tau_{\rm ref} = 3.79 t_0$ in the reference simulations to $\tau_{\rm pert} = 4.20 t_0$ in the perturbed simulations. Figures 6(a) and 6(b) show a tendency toward smaller events and larger recurrence time (events are more distant from each other) in the perturbed runs compared to the reference runs.

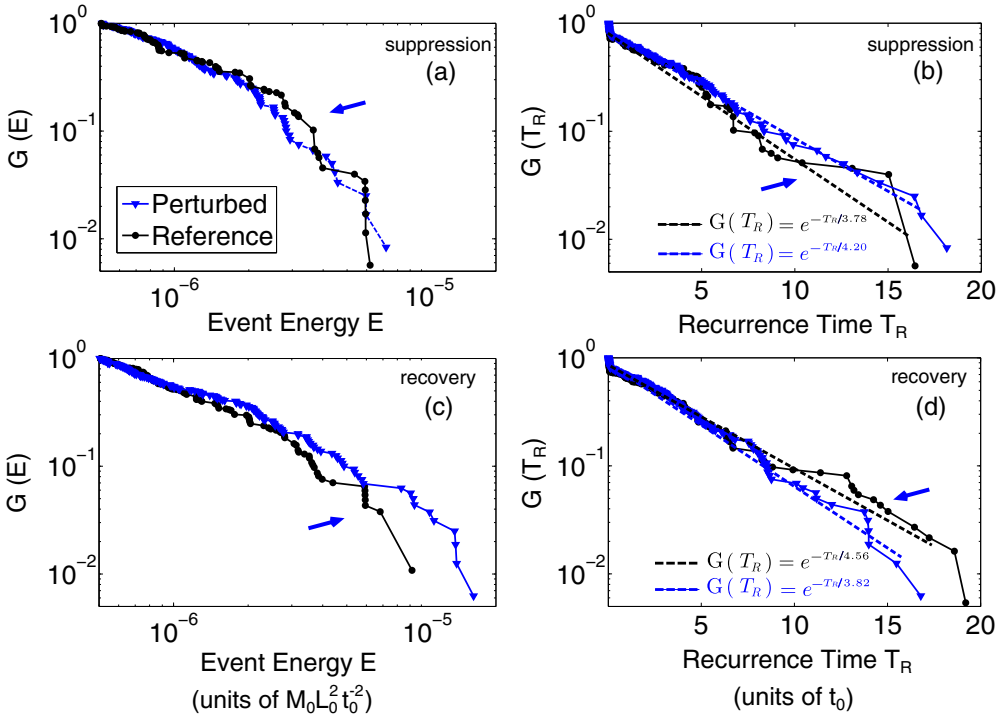

FIG. 6. (Color online) Complementary cumulative size distribution G of the (a) event energy size E and (b) recurrence time T_R for the period of energy release suppression in the perturbed and reference runs for 30 triggered large events. Also shown is the G of the (c) event energy size E and (d) recurrence time T_R for the perturbed and reference runs during the recovery period of perturbed runs. The results are for when the vibration is applied at about the middle of the stick phase for each event. The dashed lines (black for reference and blue for perturbed) in (b) and (d) show the exponential distributions of the type $G(T_R) = e^{-T_R/\tau}$, where T_R is the recurrence time and τ is the average recurrence time of the distribution. These exponential distributions are best fit to the recurrent time G. The vibration amplitude is $A = 7 \times 10^{-6} L_0$ and only events with $E \geqslant 5 \times 10^{-7} M_0 L_0^2 t_0^{-2}$ are considered in the calculations.

The distribution functions G of energy size and recurrence time during the recovery period are presented in Figs. 6(c) and 6(d), respectively. The average recurrence time τ decreases from $\tau_{\text{ref}} = 4.56 t_0$ in the reference simulations to $\tau_{\text{pert}} = 3.82 t_0$ in the perturbed simulations. Figures 6(c) and 6(d) show a shift toward larger events and smaller recurrence time (events are more closely spaced) during the recovery period in the perturbed runs compared to the reference runs.

B. Vibration close to the onset of a large slip event

The friction coefficient signal for the reference and perturbed runs of an example simulation when vibration is applied in the vicinity of the large slip event is presented in Fig. 7(a). The vibration amplitude is $A = 7 \times 10^{-6} L_0$. We observe that, upon applying vibration at this time, the triggered large slip event takes place almost at the same location as in the reference run. The kinetic energy signal in Fig. 7(b) shows that the energy release of the triggered event is less than the reference case. The cumulative energy release $\tilde{E}(t)$ for the reference and perturbed runs is presented in Fig. 7(c) and indicates the occurrence of perturbed slip events almost at its reference location with slightly lower energy release than the reference events. Figure 7(d) illustrates the difference between the cumulative energy release $\tilde{E}(t)$ of the perturbed run and that of the reference run ($\tilde{E}_{\text{pert}} - \tilde{E}_{\text{ref}}$). It indicates that, following triggering, there is a temporary interval of energy suppression in the perturbed run compared to the reference. However, this suppression, similar to when the triggering is applied at about the middle of the stick phase, is compensated for shortly after with a sequence of slip events that results in an overall higher energy release in the perturbed run compared to the reference until $t_{\text{norm}} \approx 3.2 t_0$.

Figure 7(e) shows the recurrence time for slip events with size $E \geqslant 5 \times 10^{-7} M_0 L_0^2 t_0^{-2}$ in the reference and perturbed runs. Similar to when the vibration is applied in the middle of stick phase, here also we observe that during $1 < t_{\text{norm}} < 3.2$, a sequence of slip events with smaller recurrence time takes place in the perturbed run.

The results of the triggering simulations of 30 large events selected from different independent reference runs are presented in Fig. 8. These 30 reference runs are the same as those used for the study of vibration applied in the middle of the stick phase. The results show on average a suppression of energy release in the perturbed simulations until $t_{\text{norm}} \approx 3.5$. The suppression of energy release is followed by a recovery period of higher energy release and higher activity during interval $t_{\text{norm}} = [3.5,5]$.

Figures 8(b) and 8(c) show $\frac{N_{\text{pos}}}{N_{\text{tot}}}$ and $\frac{N_{\text{neg}}}{N_{\text{tot}}}$ for the $\tilde{E}_{\text{pert}} - \tilde{E}_{\text{ref}}$ distribution across the time axis, respectively. Immediately after vibration, the probability of $\tilde{E}_{\text{pert}} - \tilde{E}_{\text{ref}} < 0$ increases abruptly to around 80%, which implies the

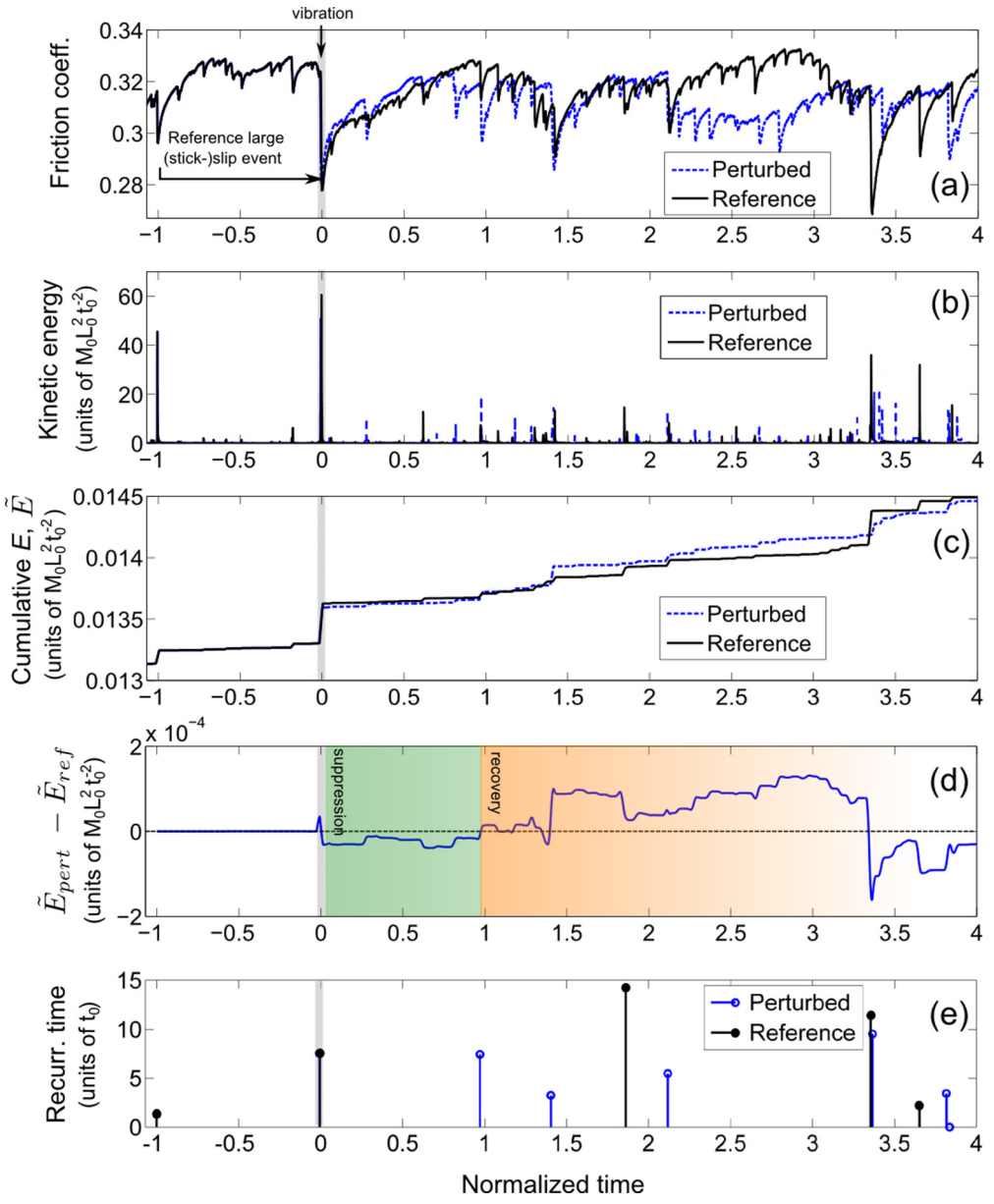

FIG. 7. (Color online) Characteristic behavior when vibration is applied slightly before a large event onset: (a) friction coefficient signal, (b) total kinetic energy signal, (c) cumulative energy release $\tilde{E}(t)$ for the reference and perturbed runs, (d) difference between the cumulative energy release of the perturbed run and that of the reference run ($\tilde{E}_{\text{pert}} - \tilde{E}_{\text{ref}}$), and (e) recurrence time for slip events with $E \geqslant 5 \times 10^{-7} M_0 L_0^2 t_0^{-2}$. The vibration amplitude is $A = 7 \times 10^{-6} L_0$.

energy suppression phenomenon. As we get farther from the vibration interval, the intensity of energy suppression decreases, while the probability of $\tilde{E}_{\text{pert}} - \tilde{E}_{\text{ref}} > 0$ increases. As we approach the recovery period, the positive and negative values of $\tilde{E}_{\text{pert}} - \tilde{E}_{\text{ref}}$ become equally abundant.

Figures 9(a) and 9(b) show the G distribution of events size [Fig. 9(a)] and recurrence time [Fig. 9(b)] for slip events with $E \geqslant 5 \times 10^{-7} M_0 L_0^2 t_0^{-2}$ during the period of suppression of the energy release in the perturbed runs and the respective time interval in the reference runs for 30 triggered large events. The average recurrence time τ increases from $\tau_{\text{ref}} = 3.95 t_0$ in the reference simulations to $\tau_{\text{pert}} = 4.73 t_0$ in the perturbed simulations. Figures 9(a) and 9(b) suggest the occurrence of smaller events with larger recurrence time in the perturbed runs compared to the reference runs, during the suppression period.

The distribution function G of energy size and recurrence time during the recovery period are presented in Figs. 9(c) and 9(d), respectively. The average recurrence time τ decreases from $\tau_{\text{ref}} = 4.69 t_0$ in the reference simulations to $\tau_{\text{pert}} = 4.08 t_0$ in the perturbed simulations. These figures show that larger events take place with smaller recurrence time in the perturbed runs compared to the reference runs.

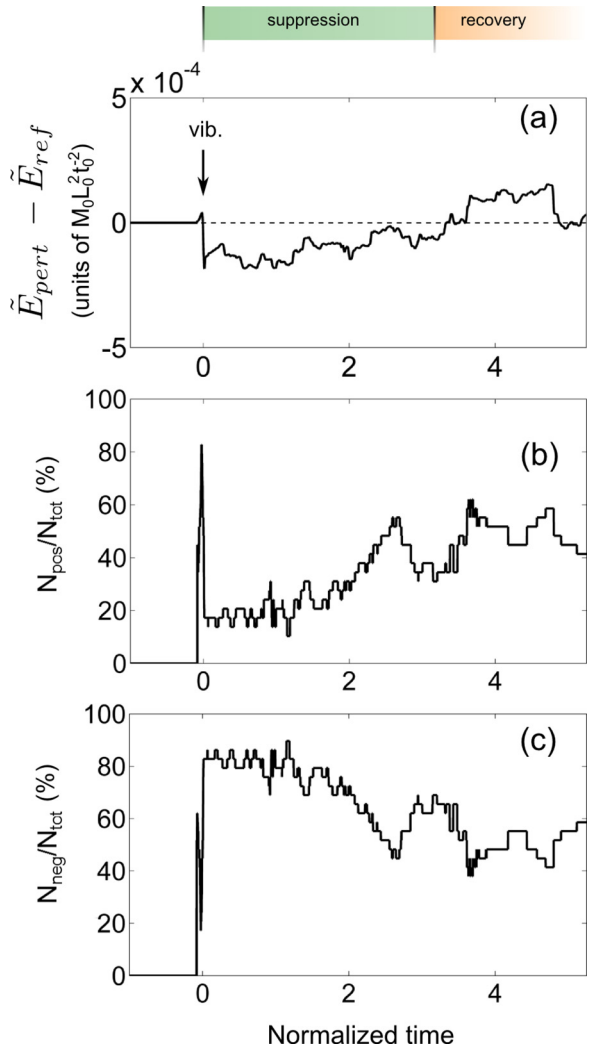

FIG. 8. (Color online) (a) Average results of the difference between the cumulative energy release of the perturbed run and that of the reference run ($\tilde{E}_{\text{pert}} - \tilde{E}_{\text{ref}}$) for 30 triggered large events when vibration is applied slightly before the onset of a large event for each case (arrow indicates the approximate location of vibration in the perturbed runs). The vibration amplitude is $A = 7 \times 10^{-6} L_0$. (b) Percentage of realizations $\frac{N_{\text{pos}}}{N_{\text{tot}}}$ where $\tilde{E}_{\text{pert}} - \tilde{E}_{\text{ref}} > 0$. (c) Percentage of realizations $\frac{N_{\text{neg}}}{N_{\text{tot}}}$ where $\tilde{E}_{\text{pert}} - \tilde{E}_{\text{ref}} < 0$.

IV. DISCUSSION AND OUTLOOK

Our investigation shows that large enough vibration amplitudes $A \geqslant 6 \times 10^{-6} L_0$ cause a significant clock advance of an upcoming large slip event in a sheared granular layer similar to the experiments of Johnson *et al.* and in some studies in the earth [4,26,59]. We observe that the perturbed runs show a significant decrease of the slipping contact ratio R_{SC} toward the end of the vibration interval and shortly after it terminates. The decrease of the slipping contact ratio is followed by a slow recovery to its reference value after the removal of vibration, if the vibration amplitude is $A < 6 \times 10^{-6} L_0$. The dependence of this recovery time on the shear rate should be further investigated. If $A \geqslant 6 \times 10^{-6} L_0$, the R_{SC} value decreases to its initial level at the beginning of the stick phase and does not recover to the reference trajectory. The decrease of R_{SC} to a value at the beginning of the stick phase suggests that the medium is unable to sustain its current high shear stress level and we subsequently observe a significant clock advance of the slip event for these cases. The significant change of the R_{SC} is believed to be accompanied by a weakening of the granular medium expressed by a reduction of its shear modulus. This follows the hypothesis proposed in [18,20] about the change of the shear modulus of the granular layer following large enough acoustic perturbations.

The suppression of the energy release when vibration is applied in the middle of the stick phase is due to the fact that the large event takes place with a clock advance (earlier) in the stick phase. This means that less energy is stored in the granular layer and a smaller event, accompanied by temporary energy release suppression, is expected. The following recovery period of increased energy release and higher activity in the granular layer is then expected from the energy conservation point of view. One has to remember that energy is continuously supplied to the system by the shear load. As a consequence of this continuous supply, one can think of a sort of energy conservation within the system.

The distributions of $\tilde{E}_{\text{pert}} - \tilde{E}_{\text{ref}}$ for 30 realizations show an abrupt increase of the negative values shortly after the reference event location for both cases, when vibration is applied either in the middle of the stick phase or close to the event onset. This implies the significance of the energy suppression influence after triggering. The suppression influence is followed by a recovery period of higher energy release and increased activity in the granular layer, during which the probability of $\tilde{E}_{\text{pert}} - \tilde{E}_{\text{ref}} > 0$ constantly increases, until it reaches and fluctuates around 50%, hence equal to the probability of $\tilde{E}_{\text{pert}} - \tilde{E}_{\text{ref}} < 0$. It would be useful to investigate the evolution of the granular layer properties including its shear and compression moduli during these two intervals.

In earth, dynamically triggered earthquakes seldom occur instantaneously but often with some delay, long after the triggering strain has passed [7,9,60]. In addition, a period of increased seismicity has been observed and sustained for days to weeks in some delayed triggering scenarios [6]. The energy suppression and the subsequent recovery, consisting of higher energy release and increased activity period in our DEM model, can explain the abundance of observations that support delayed dynamically triggered events in the earth as well as the difficulty and possible controversies in the identification of (dynamically) triggered earthquakes [61,62].

An increase in the density of larger events (events with moment magnitude $M \geqslant 5$) following the dynamic triggering by the 11 April 2012 east Indian Ocean earthquake has been reported for distant triggered earthquakes globally as well as in individual regions, for example, the Gulf of California [59]. This change, associated with the DET phenomenon, also involves an increase in the seismicity rate (or equivalently a decrease in the recurrence time) of events with moment magnitude $M \geqslant 5$ in the individual triggered regions as well as distant triggered regions worldwide [59]. The decrease in the recurrence time has also been reported for experiments of acoustic slip triggering in sheared granular layers by Johnson *et al.* [21].

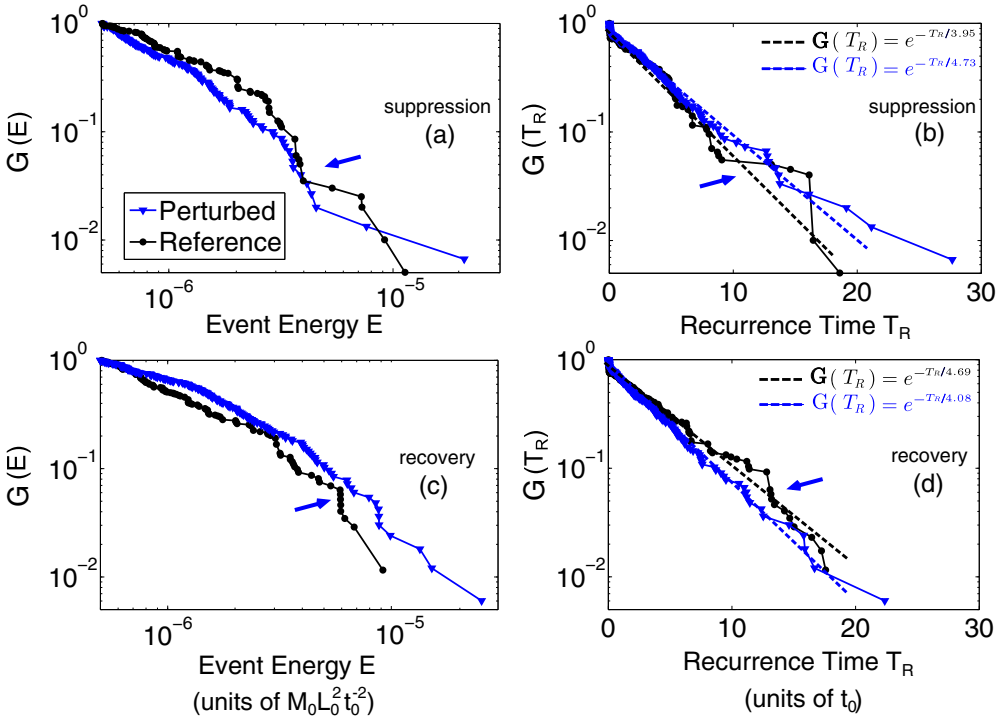

FIG. 9. (Color online) Complementary cumulative distribution function G of (a) event energy size E and (b) recurrence time T_R for the period of higher energy release in the perturbed runs and their respective periods in the reference runs for 30 triggered large events. Also shown is the G of (c) event energy size E and (d) recurrence time T_R for the perturbed and reference runs during the period of higher energy release in the perturbed runs and the respective time periods in the reference runs. The results are for when the vibration is applied slightly before the onset of a large event for each case. The dashed lines (black for reference and blue for perturbed) in (b) and (d) show the exponential distributions of the type $G(T_R) = e^{-T_R/\tau}$, where T_R is the recurrence time and τ is the average recurrence time of the distribution. The vibration amplitude is $A = 7 \times 10^{-6} L_0$ and only events with $E \geqslant 5 \times 10^{-7} M_0 L_0^2 t_0^{-2}$ are considered in the calculations.

V. CONCLUSION

In this work we investigated the influence of boundary vibration on stick-slip dynamics of sheared granular layers. We used a range of vibration amplitudes for slip triggering and show that above a critical amplitude $A \geqslant 6 \times 10^{-6} L_0$, vibration and dynamic stressing cause a significant clock advance of large stick-slip events. We linked the observed clock advance for $A \geqslant 6 \times 10^{-6} L_0$ to a major decline in the slipping contact ratio R_{SC} of the granular gouge layer and showed that in these cases the R_{SC} cannot recover to its reference trajectory. We used the triggering amplitude to investigate the size of the triggered slips (in terms of energy release during slip) and its evolution for two cases: (i) vibration applied at about the middle of the stick phase and (ii) vibration applied close to the event onset. In both cases, we observed a suppression of energy release in the perturbed simulations, in the short term after vibration. For the case when vibration is applied at the middle of the stick phase, a significant clock advance of the large slip event occurs. In the long term after vibration, there is more energy release and higher activity in the perturbed run, which compensates for the temporary suppression of energy release within the short term after vibration. The energy suppression and the subsequent recovery, higher energy release, and increased activity period in our DEM model can explain the abundance of observations that support delayed dynamically triggered events in the earth as well as the difficulties in the identification of triggered earthquakes.

ACKNOWLEDGMENTS

We thank D. Weatherley and S. Abe for support during the implementation of our DEM model in the ESYS-PARTICLE code and D. Passerone and C. Pignedoli for help related to the use of the high-performance computing cluster Ipazia at EMPA. Our work was supported by the Swiss National Science Foundation (Projects No. 206021-128754 and No. 200021-135492) and by the LDRD Program (Institutional Support) at the Los Alamos National Laboratory, USA. We thank two anonymous reviewers for their insightful comments, which helped us improve the manuscript.

[1] W. F. Brace and J. D. Byerlee, Science **153**, 990 (1966).
[2] W. F. Brace and J. D. Byerlee, Science **168**, 1573 (1970).
[3] T. Johnson, F. T. Wu, C. H. Scholz, and S. Url, Science **179**, 278 (1973).
[4] J. Gomberg, P. A. Reasenberg, P. Bodin, and R. A. Harris, Nature (London) **411**, 462 (2001).
[5] J. Gomberg, P. Bodin, K. Larson, and H. Dragert, Nature (London) **427**, 621 (2004).

[6] D. R. Shelly, Z. Peng, D. P. Hill, and C. Aiken, Nat. Geosci. **4**, 384 (2011).
[7] A. A. Velasco, S. Hernandez, T. Parsons, and K. Pankow, Nat. Geosci. **1**, 375 (2008).
[8] D. Marsan and O. Lengline, Science **319**, 1076 (2008).
[9] A. M. Freed, Annu. Rev. Earth Planet. Sci. **33**, 335 (2005).
[10] C. H. Scholz, *The Mechanics of Earthquakes and Faulting* (Cambridge University Press, Cambridge, 2002).
[11] K. E. Daniels and N. W. Hayman, J. Geophys. Res. **113**, 1 (2008).
[12] N. W. Hayman, L. Ducloué, K. L. Foco, and K. E. Daniels, Pure Appl. Geophys.**168**, 2239 (2011).
[13] S. Luding, E. Clement, A. Blumen, J. Rajchenbach, and J. Duran, Phys. Rev. E **49**, 1634 (1994).
[14] H. M. Savage and C. Marone, J. Geophys. Res. **113**, 1 (2008).
[15] A. Janda, D. Maza, A. Garcimartín, J. Lanuza, and E. Clément, Europhys. Lett. **87**, 24002 (2009).
[16] R. Capozza, A. Vanossi, A. Vezzani, and S. Zapperi, Phys. Rev. Lett. **103**, 085502 (2009).
[17] M. F. Melhus, I. S. Aranson, D. Volfson, and L. S. Tsimring, Phys. Rev. E **80**, 041305 (2009).
[18] X. Jia, T. Brunet, and J. Laurent, Phys. Rev. E **84**, 020301(R) (2011).
[19] K. Xia, S. Huang, and C. Marone, Geochem. Geophys. Geosyst. **14**, 1012 (2013).
[20] P. A. Johnson and X. Jia, Nature (London) **437**, 871 (2005).
[21] P. A. Johnson, H. Savage, M. Knuth, J. Gomberg, and C. Marone, Nature (London) **451**, 57 (2008).
[22] C. Marone, Annu. Rev. Earth Planet. Sci. **94**, 17691 (1998).
[23] C. Marone, Nature (London) **391**, 69 (1998).
[24] K. Mair and C. Marone, J. Geophys. Res. **104**, 889 (1999).
[25] J. L. Anthony and C. Marone, J. Geophys. Res. **110**, 1 (2005).
[26] J. Gomberg and P. A. Johnson, Nature (London) **437**, 830 (2005).
[27] N. J. van der Elst and E. Brodsky, J. Geophys. Res. **115**, B07311 (2010).
[28] D. Pasqualini, T. Heitmann, J. A. TenCate, S. Habib, D. Higdon, and P. A. Johnson, J. Geophys. Res. **112**, B01204 (2007).
[29] J. A. TenCate, D. Pasqualini, S. Habib, K. Heitmann, D. Higdon, and P. A. Johnson, Phys. Rev. Lett. **93**, 065501 (2004).
[30] M. L. Falk and J. S. Langer, Phys. Rev. E **57**, 7192 (1998).
[31] B. A. DiDonna and T. C. Lubensky, Phys. Rev. E **72**, 066619 (2005).
[32] M. Griffa, B. Ferdowsi, E. G. Daub, R. A. Guyer, P. A. Johnson, C. Marone, and J. Carmeliet, Philos. Mag. **92**, 3520 (2012).
[33] M. Griffa, E. G. Daub, R. A. Guyer, P. A. Johnson, C. Marone, and J. Carmeliet, Europhys. Lett. **96**, 14001 (2011).
[34] M. Griffa, B. Ferdowsi, R. A. Guyer, E. G. Daub, P. A. Johnson, C. Marone, and J. Carmeliet, Phys. Rev. E **87**, 012205 (2013).
[35] B. Ferdowsi, M. Griffa, R. A. Guyer, P. A. Johnson, and J. Carmeliet, Acta Mech., doi:10.1007/s00707-014-1136-y.
[36] P. Johnson, B. Ferdowsi, B. Kaproth, M. Scuderi, M. Griffa, J. Carmeliet, R. Guyer, P.-Y. Le Bas, D. Trugman, and C. Marone, Geophys. Res. Lett. **40**, 5627 (2013).
[37] A. P. Rathbun, F. Renard, and S. Abe, J. Geophys. Res. **118**, 878 (2013).
[38] D. Place and P. Mora, J. Comput. Phys. **150**, 332 (1999).
[39] Y. Wang, S. Abe, S. Latham, and P. Mora, Pure Appl. Geophys. **163**, 1769 (2006).
[40] C. Marone, B. M. Carpenter, and P. Schiffer, Phys. Rev. Lett. **101**, 248001 (2008).
[41] B. Ferdowsi, M. Griffa, R. A. Guyer, P. A. Johnson, C. Marone, and J. Carmeliet, Geophys. Res. Lett. **40**, 4194 (2013).
[42] P. A. Cundall and O. D. L. Strack, Geotechnique **29**, 47 (1979).
[43] M. P. J. Schoepfer, S. Abe, C. Childs, and J. Walsh, Int. J. Rock Mech. Min. Sci. **46**, 250 (2009).
[44] E. Aharonov and D. Sparks, Phys. Rev. E **60**, 6890 (1999).
[45] Y. Wang, Acta Geotech. **4**, 117 (2009).
[46] H. Kanamori and D. L. Anderson, Bull. Seismol. Soc. Am. **65**, 1073 (1975).
[47] A. A. Kagan, Geophys. J. Int. **106**, 123 (1991).
[48] C. Godano and F. Pingue, Geophys. J. Int. **142**, 193 (2000).
[49] E. Aharonov and D. Sparks, J. Geophys. Res. **109**, B09306 (2004).
[50] K. Shundyak, M. van Hecke, and W. van Saarloos, Phys. Rev. E **75**, 010301 (2007).
[51] C. Song, P. Wang, and H. A. Makse, Nature (London) **453**, 629 (2008).
[52] D. Bi, J. Zhang, B. Chakraborty, and R. P. Behringer, Nature (London) **480**, 355 (2011).
[53] P. Cundall, in *Proceedings of the Fourth International Conference on Numerical Methods in Geomechanics, Edmonton, 1982*, edited by Z. Eisenstein (CRC/Balkema, Leiden, 1982), p. 23.
[54] C. Thornton, Geotechnique **50**, 43 (2000).
[55] C. O'Sullivan and J. D. Bray, Eng. Comput. **21**, 278 (2004).
[56] G. MiDi, Eur. Phys. J. E **14**, 341 (2004).
[57] I. Agnolin and J.-N. Roux, Phys. Rev. E **76**, 061302 (2007).
[58] Y. Sheng, C. Lawrence, B. Briscoe, and C. Thornton, Eng. Comput. **21**, 304 (2004).
[59] F. F. Pollitz, R. S. Stein, V. Sevilgen, and R. Bürgmann, Nature (London) **490**, 250 (2012).
[60] D. P. Hill, Science **260**, 1617 (1993).
[61] K. Richards-Dinger, R. S. Stein, and S. Toda, Nature (London) **467**, 583 (2010).
[62] K. R. Felzer and E. E. Brodsky, Nature (London) **441**, 735 (2006).